PHYSICAL REVIEW B **73**, 045129 (2006)

Orientation-dependent electron-energy-loss spectroscopy of TiO_2: A comparison of theory and experiment

Christian Heiliger,[1,2,*] Frank Heyroth,[2] Frank Syrowatka,[2] Hartmut S. Leipner,[2] Igor Maznichenko,[3] Kalevi Kokko,[4] Wolfram Hergert,[1] and Ingrid Mertig[1]
[1]*Department of Physics, Martin Luther University, D-06099 Halle, Germany*
[2]*Interdisciplinary Center of Materials Science, Martin Luther University, Hoher Weg 8, D-06120 Halle, Germany*
[3]*Theoretical Department of Institute of Physics, Rostov State University, 194, Stachky Ave., 344090 Rostov-on-Don, Russia*
[4]*Department of Physics, University of Turku, FIN-20014 Turku, Finland*

(Received 5 March 2004; revised manuscript received 19 October 2005; published 27 January 2006)

We present a comparison of calculated and measured orientation-dependent electron-energy-loss spectroscopy (EELS) spectra of TiO_2. The measurements were carried out with a scanning transmission microscope equipped with a parallel EELS detector. The lateral resolution is about 1 nm and the energy resolution is about 0.3–0.4 eV. The calculations are based on density functional theory. Spin-orbit coupling is included in the theoretical description of the core levels. Many-body corrections are included by a $Z+1$ approximation. The influence of experimental parameters like the collector and divergence semiangles are discussed in detail. Very good agreement between theoretical and experimental results concerning the peak positions of the spectra is reached by means of the $Z+1$ approximation. The investigated rutile, anatase, and brookite modifications exhibit pronounced differences in the L_3 edge of titanium. The orientation dependence is clearly visible in the oxygen K edge.

DOI: 10.1103/PhysRevB.73.045129 PACS number(s): 79.20.Uv, 34.80.−i, 71.15.Qe, 71.20.−b

I. INTRODUCTION

Modern electron-energy-loss spectroscopy (EELS) is capable of providing experimental results comparable to x-ray absorption spectroscopy (XAS). The advantage of EELS measured in a transmission electron microscope (TEM) is the additional high lateral resolution down to 0.2 nm with 500 meV and 2 nm with 100 meV energy resolution.[1] The fine structure within a few electron-volts (eV) above the onset of an edge is the electron-energy-loss near-edge structure (ELNES) comparable to x-ray absorption near edge structure (XANES). This fine structure reflects the unoccupied electron states.

Fingerprint methods are quite often used for chemical analysis. For this purpose, reference spectra are averaged over all crystallographic orientations.[2] The aim of our paper is to investigate the orientation dependence of the spectra and to analyze the influence of chemical bonding. For this reason, we chose TiO_2, which exists in three modifications rutile, anatase, and brookite having slightly different bonding conditions. Most of the experimental[3] and theoretical[4–6] investigations dealing with the orientation dependence consider either the part of the momentum transfer parallel or perpendicular to the orientation of the sample surface. In this paper we analyze the angular distribution of a spectrum.

For the theoretical description of EELS, different *ab initio* methods based on density functional theory[6–11] (DFT) have been applied. A review is given in Ref. 12. The theoretical description of XAS is in its basic aspects also similar to EELS.[2]

II. ELNES

The double differential cross section σ can be obtained by Fermi's Golden Rule within the Born approximation[13]

$$\frac{\partial^2\sigma}{\partial E\partial\Omega} = \frac{4}{a_0^2}\frac{k'}{k_0}\frac{1}{q^4}|\langle f|e^{i\mathbf{q}\cdot\mathbf{r}}|i\rangle|^2\delta(E+E_f-E_i). \quad (1)$$

k_0 and k' are the wave numbers of the incident and scattered fast electrons, and $\mathbf{q}=\mathbf{k}_0-\mathbf{k}'$ is the momentum transfer. $\langle f|$ and $|i\rangle$ indicate the final and the initial states of the excited electron within the atom in a one-electron picture with the corresponding energies E_f and E_i. a_0 is the Bohr radius, Ω is the solid scattering angle, $\mathbf{r}$ is the position vector, and E is the energy. This formula for the cross section was derived by Bethe.[14] The important part of the cross section is the transition matrix element assuming energy conservation. This part is also called dynamic form factor[6] (DFF) S,

$$S(\mathbf{q},E) = \sum_{i,f}|\langle f|e^{i\mathbf{q}\cdot\mathbf{r}}|i\rangle|^2\delta(E+E_f-E_i), \quad (2)$$

and will be discussed below in more detail. There exist extensions of this factor to include relativistic effects[15] or the generalization to the mixed dynamic form factor (MDFF).[16] Since we are using incident electrons with an energy of 100 keV, relativistic effects[15] will be neglected in first order beside spin-orbit coupling of the initial states.

A. Orientation dependence of ELNES

We consider the excitation of a strongly bound core electron. That is, the initial state $|i\rangle$ is a core state and can be separated into a radial function ϕ depending on the main quantum number n, the orbital angular momentum l_c, the total angular momentum j, magnetic quantum number m_j, and an angular contribution $\tilde{Y}$ depending on $\hat{\mathbf{r}}=\mathbf{r}/r$,

$$\langle \mathbf{r}|i\rangle = \phi^{c}_{nl_cj}(r)\langle \mathbf{r}|jl_cm_j\rangle = \phi^{c}_{nl_cj}(r)\tilde{Y}^{l_c}_{jm_j}(\hat{\mathbf{r}}). \qquad (3)$$

c indicates the core state. In contrast to Nelhiebel *et al.*,[6] the spin orbit coupling of the core levels is taken into account in this paper. Therefore, the angular part has to be expanded into spherical harmonics in terms of orbital angular momenta l_c and m_c, and into eigenfunctions of the spin state m_{s_c},

$$\langle \mathbf{r}|i\rangle = \phi^{c}_{nl_cj}(r)\sum_{m_c,m_{s_c}}\left\langle l_cm_c\tfrac{1}{2}m_{s_c}\middle|jm_j\right\rangle Y^{l_c}_{m_c}(\hat{\mathbf{r}})\left\langle \mathbf{r}\middle|\tfrac{1}{2}m_{s_c}\right\rangle. \qquad (4)$$

$\left\langle l_cm_c\tfrac{1}{2}m_{s_c}\middle|jm_j\right\rangle$ represents the Clebsch-Gordan coefficients of the expansion. The final state $|f\rangle$ is a band state, which can be represented by wave functions localized to atoms and a coefficient C depending on the wave vector $\mathbf{k}$, band index ν, spin moment m_s, and the orbital angular momenta l and m,

$$|f\rangle = \sum_{lm} C^{\mathbf{k}\nu}_{lmm_s}|f^{\mathrm{atom}}_{lmm_s}\rangle. \qquad (5)$$

With respect to the assumed spherical symmetry of the potential at the atomic site, the atomiclike wave functions can also be separated into a radial and an angular contribution

$$\langle \mathbf{r}|f^{\mathrm{atom}}_{lmm_s}\rangle = \phi^{v}_{lm_s}(r)Y^{l}_{m}(\hat{\mathbf{r}})\left\langle \mathbf{r}\middle|\tfrac{1}{2}m_s\right\rangle. \qquad (6)$$

v indicates the valence state. Expanding the interaction operator into spherical harmonics, depending on the angular parts $\hat{\mathbf{q}}$ and $\hat{\mathbf{r}}$, and the spherical Bessel function J,

$$e^{i\mathbf{q}\cdot\mathbf{r}} = 4\pi\sum_{\lambda=0}^{\infty}\sum_{\mu=-\lambda}^{\lambda} i^{\lambda}Y^{\lambda}_{\mu}(\hat{\mathbf{q}})^{*}Y^{\lambda}_{\mu}(\hat{\mathbf{r}})J_{\lambda}(qr), \qquad (7)$$

and using the $3j$ symbols,[13] represented by 3×2 matrices, one can obtain the main result for the DFF,

$$\begin{aligned}S(\mathbf{q},E) = {} & 4\pi(2l_c+1)\sum_{m_s}\sum_{l}\sum_{l'}\sum_{m=-l}^{l}\sum_{m'=-l'}^{l'}(-1)^{m+m'}i^{-l+l'}\sqrt{2l+1}\sqrt{2l'+1}\sum_{\lambda=0}^{\infty}\sum_{\lambda'=0}^{\infty}i^{\lambda-\lambda'}\sqrt{2\lambda+1}\sqrt{2\lambda'+1}R^{cv}_{\lambda nl_cjlm_s}(q)R^{cv}_{\lambda' nl_cjl'm_s}(q)\\ & \times\begin{pmatrix} l & \lambda & l_c\\ 0 & 0 & 0\end{pmatrix}\begin{pmatrix} l' & \lambda' & l_c\\ 0 & 0 & 0\end{pmatrix}\sum_{m_c=-l_c}^{l_c}\left|\left\langle l_cm_c\tfrac{1}{2}m_s\middle|jm_j\right\rangle\right|^2\sum_{\mu=-\lambda}^{\lambda}\sum_{\mu'=-\lambda'}^{\lambda'}Y^{\lambda}_{\mu}(\hat{\mathbf{q}})^{*}Y^{\lambda'}_{\mu'}(\hat{\mathbf{q}})\begin{pmatrix} l & \lambda & l_c\\ -m & \mu & m_c\end{pmatrix}\\ & \times\begin{pmatrix} l' & \lambda' & l_c\\ -m' & \mu' & m_c'\end{pmatrix}\sum_{\mathbf{k}\nu}(C^{\mathbf{k}\nu}_{lmm_s})^{*}C^{\mathbf{k}\nu}_{l'm'm_s}\delta(E+E_f-E_i). \end{aligned} \qquad (8)$$

To derive this equation, the orthogonality relation of spin states is applied. The radial integral is given by

$$R^{cv}_{\lambda nl_cjlm_s}(q) := \int drr^2J_{\lambda}(qr)\phi^{c}_{nl_cj}(r)\phi^{v}_{lm_s}(r). \qquad (9)$$

The main difference in comparison to the result of Nelhiebel *et al.*[6] is the additional Clebsch-Gordan coefficient due to the inclusion of the spin-orbit coupling of the core states. This coefficient is very important for the distinction between L_2 and L_3 edges. Both edges are related to the excitation of a $2p$ electron with different total angular momentum j.

The dipole selection rules are fulfilled by $\lambda=\lambda'=1$. The high energy of the incoming electron beam of 100 keV guarantees the validity of the dipole selection rules.[17] Therefore, it is not necessary to sum up over all values of λ but using only $\lambda=1$.

B. Influence of the scattering geometry

In Fig. 1, the scattering geometry for different experimental setups with different values of collector and divergence semiangles are shown. How these angles are obtained is discussed below. The gray surfaces of the cones represent all possible values of $\mathbf{k}_0$ and $\mathbf{k}'$. The magnitude of the momentum transfer $\mathbf{q}=\mathbf{k}_0-\mathbf{k}'$ is shown in Fig. 2 as a function of the angle between $\mathbf{q}$ and $\mathbf{k}'$. The surface normal vector of the sample is parallel to $\mathbf{k}'$. The magnitude of the momentum transfer is calculated for an equidistant mesh in the basis plane of the cone with a 13 mrad collector semiangle and a 28 mrad divergence semiangle (imaging mode). The result demonstrates that we average nearly over all orientations in the sample but with different weight. Within the dipole ap-

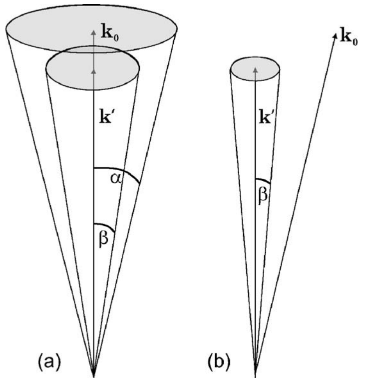

FIG. 1. Relation of the wave vectors $\mathbf{k}_0$ and $\mathbf{k}'$ for the two experimental setups. (a) Imaging mode with a collector semiangle $\beta=13$ mrad and a divergence semiangle $\alpha=28$ mrad and (b) diffraction mode with $\beta=3.3$ mrad and $\alpha<10^{-2}$ mrad.

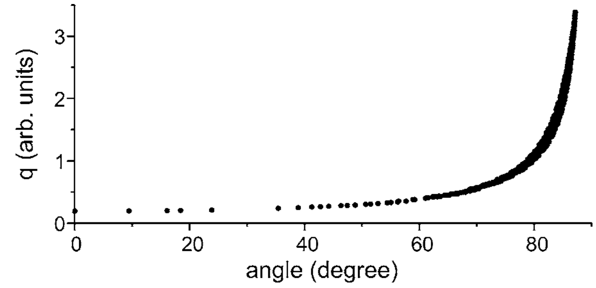

FIG. 2. Possible values for the momentum transfer q vs the angle ϕ between $\mathbf{k}'$ and $\mathbf{q}$ for a collector semiangle of 13 mrad and a divergence semiangle of 28 mrad.

proximation, the intensity decreases with q^{-2} [see Eq. (1)]. Consequently, the vectors $\mathbf{q}$ at high angles ϕ contribute only a small amount of intensity to the whole spectrum, although the number of vectors $\mathbf{q}$ is much larger. Therefore we introduce a center of intensity $\bar{\phi}$,

$$\bar{\phi} = \frac{\int_0^\pi q(\phi)^{-2}\phi\, d\phi}{\int_0^\pi q(\phi)^{-2} d\phi}. \tag{10}$$

In our example (Fig. 2), the center of intensity is calculated to be about 67°. Therefore, the obtained spectrum includes more information about directions perpendicular to $\mathbf{k}'$, that is, perpendicular to the surface normal, which is along the crystallographic c or a axis. For this reason, we expect a weak orientation dependence in this mode.

In order to obtain a pronounced orientation dependence it is necessary to shift the center of intensity to lower or larger angles. The critical value for the orientation dependence is the deviation from 45°. The diffraction mode leads to a reduction in the divergence semiangle [Fig. 1(b)], but causes a loss in the lateral resolution of about 1 nm down to the order of 1 μm. The advantage of this mode is that one can tilt the beam under the sample and one can get vectors $\mathbf{q}$ at larger angles ϕ. This means that one shifts the center of intensity to larger values and the momentum transfer in the direction of the surface normal. In this mode, the orientation dependence is expected to be very pronounced. In Fig. 3 the center of intensity is shown as a function of the tilt angle of the incident electron beam for different collector semiangles. In our measurements we used a collector semiangle of 3.3 mrad and a typical tilt angle of 10 mrad. Therefore, the center of intensity was at an angle of 80°, indicating that the orientation dependence of the spectra should be pronounced in this setup.

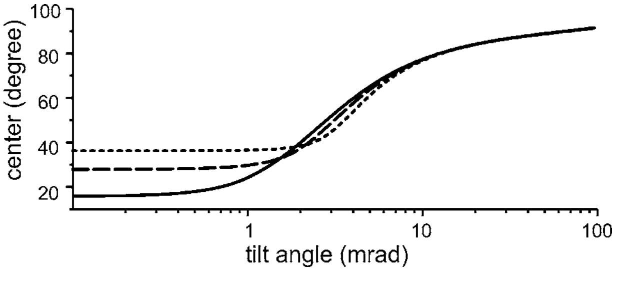

FIG. 3. The center of intensity vs the tilt angle of the incoming electron beam (angle between $\mathbf{k}_0$ and $\mathbf{k}'$) for different collector semiangles: solid line: 1 mrad, dashed line: 2 mrad, and dotted line: 3 mrad.

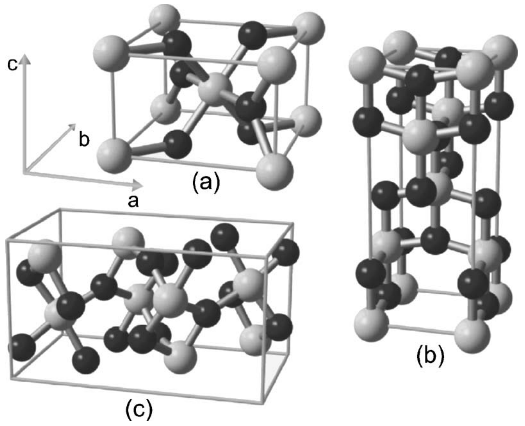

FIG. 4. TiO_2 crystal modifications: (a) rutile, (b) anatase, and (c) brookite.

III. SAMPLES

TiO_2 exists in three different crystal modifications: rutile, anatase, and brookite. The lattice structures are shown in Fig. 4. The lattice constants used and the resulting Ti-O bond length are listed in Table I. In rutile and anatase, the TiO_6 binding octahedra are slightly distorted with two different Ti-O binding lengths and different O-Ti-O binding angles. The distortion in anatase is larger than in rutile. Brookite is the most complicated structure with six different Ti-O binding lengths and 12 different O-Ti-O binding angles.[19] The band structure of rutile and anatase has been calculated quite often.[20–23] The results of brookite are rare. A theoretical investigation of the band structure, the density of states (DOS), and the lattice constants of all three modifications is given by Mo and Ching.[19]

The experimental investigations have been performed with a commercially available rutile single crystal and naturally grown anatase and brookite single crystals. Standard preparation techniques for the thinning of TEM samples, such as dimpling followed by ion polishing, have been applied. The thickness of the samples was about 0.6–0.8 of the electron mean free path.

IV. EXPERIMENTAL TREATMENT

The measurements were carried out with the scanning electron microscope VG HB 501 UX. This ultrahigh vacuum microscope is equipped with a field emission gun and works at an acceleration voltage of 100 kV. The lateral resolution amounts to about 1 nm. The microscope is equipped with the Gatan Enfina parallel EELS detector having an energy resolution of about 0.3–0.4 eV.

TABLE I. Crystal structure data of the three crystal modifications of TiO_2.

	Rutile	Anatase	Brookite
Crystal structure	Tetragonal	Tetragonal	Orthorombic
Lattice constants (Å)[a]	$a=b=4.5929$	$a=b=3.785$	$a=9.166$
			$b=5.436$
	$c=2.9591$	$c=9.514$	$c=5.135$
Space group[a]	136, $P4_2/mnm$	141, $I4_1/amd$	61, $Pbca$
Atoms per cell	6	6	24
Basis coordinates in units	Ti: 0.0 0.0 0.0	Ti: 0.0 0.0 0.0	Ti: 0.127 0.113 0.873
of the lattice constants[a]	O: 0.3056 0.3056 0.0	O: 0.0 0.0 0.2064	O_1: 0.010 0.155 0.180
			O_2: 0.230 0.105 0.535
Ti-O bond length (Å)	1.945 (4×)	1.937 (4×)	1.92 up to 1.98
	1.985 (2×)	1.964 (2×)	
O-Ti-O bond angle	81.0°	77.6°	77° up to 100°
	90.0°	92.6°	

[a] See Ref. 18.

The apertures used in the imaging mode were calibrated with images in the diffraction mode. This calibration gives a divergence semiangle of the incident beam of 28 mrad and a collector semiangle of 13 mrad.

Using the diffraction mode to obtain the spectra leads to a divergence semiangle of less than 10^{-2} mrad. An additional aperture between the sample and the spectrometer gives a collector semiangle of about 3.3 mrad. Figure 5 shows a diffraction pattern of the rutile sample oriented in the [100] direction. Out of such an image, we extract the necessary angle calibration by using the known angles of diffraction. With these calibrations, one can measure the collector and the divergence semiangle by imaging the apertures in the diffraction mode and can control the tilt angle of the beam, which is a specific feature in the diffraction mode of EELS measurements. Tilting the beam gives spectra arising mainly from a direction, which is determined by $\mathbf{k}_0$, nearly perpendicular to the normal vector of the sample surface directed in the direction of $\mathbf{k}'$, which is the microscope axis. For this reason one can measure all different perpendicular orientations simply by tilting $\mathbf{k}_0$.

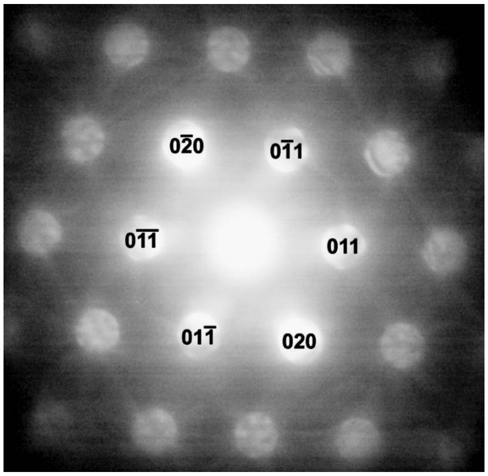

FIG. 5. Diffraction pattern of rutile oriented in [100].

The multiple scattering background of the measured spectra was subtracted with the help of a polynomial fit.[2] A deconvolution of the spectra with the low loss region was not applied, because of the very thin samples which means that there are almost single scattering processes. For the same reason other corrections like the one mentioned by Batson *et al.*[24] are not included.

V. THEORETICAL TREATMENT

The Stuttgart LMTO-47 package[25] was used to calculate the band structure. The muffin tin ASA radii used were 2.437 a.u. (rutile), 2.407 a.u. (anatase), 2.380 a.u. (brookite) for titanium, 1.863 a.u. (rutile), 1.840 a.u. (anatase), 1.830 a.u. (brookite) for oxygen. The maximum orbital momentum was $l=2$. Convergence was tested for a higher orbital momenta in rutile. No major differences in the spectra were found. Additional empty spheres had to be added: eight per primitive unit cell for rutile, 10 for anatase, and 36 for brookite. The calculation of the ELNES including the influence of the scattering geometry discussed above was implemented in the XSPEC package.[26] The differential cross section as a function of momentum transfer $\mathbf{q}$ was calculated using Eqs. (1) and (8). In order to obtain the spectra, we integrated over all possible values of $\mathbf{q}$.

An important many particle effect is the influence of the core hole, due to the fact that a hole is created if a core electron is excited. Several papers discuss the influence of the core hole,[27–29] and different approximations were developed to describe this effect.[7] The most common ones are the $Z+1$ approximation, where the excited atom with the atomic number Z is replaced by an atom with a nuclear charge of $Z+1$, and the core hole approximation, where the core level of the excited atom is unoccupied. Using these approaches, another ground state is calculated within the DFT. The problem of this approximation is that an extra valence electron, which influences the unoccupied states and therefore the spectrum, is added due to charge neutrality.

For the calculation of K edges, the $Z+1$ approximation as well as the core hole approximation give good agreement

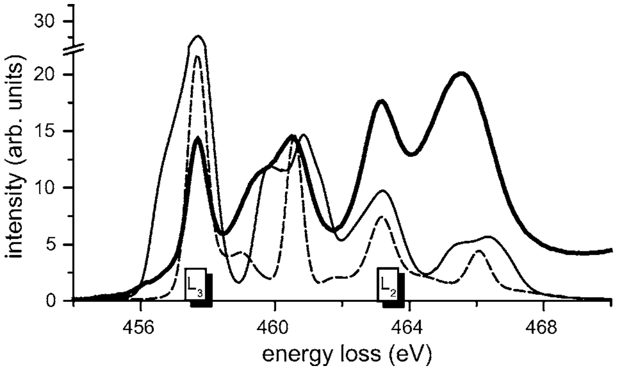

FIG. 6. Calculations of the titanium L edges of rutile without consideration of the core hole (thin solid line) and using a $Z+1$ approximation (dashed line) in comparison to experimental data (thick solid line) obtained in the imaging mode. The sample surface is oriented in [100].

with experiments.[30,31] The treatment of the core hole for L edges, where the electron is excited from a $2p$ state, is more complicated. Multiplet methods[32–34] have been successfully used to calculate L spectra. The treatment of the core hole in L edges within the DFT was also studied.[29,35] The $Z+1$ approximation yields good results for silicon L edges.[29] For copper L edges Luitz *et al.*[36] achieved the best agreement using 1/2 of a core hole. For transition metal oxides the best agreement with the experiment is achieved by treating the whole core hole.[35] In conclusion, the treatment of the core hole is often used to adapt the theoretical results to the experimental data.[35]

In Fig. 6, the calculations for rutile are shown without core hole and within a $Z+1$ approximation. The parameters of the imaging mode, in comparison to experimental data of rutile in [100] direction of the sample surface are used. The first peak of the L_3 edge is not very well described without the core hole. This is improved by the consideration of the core hole, which leads to narrower $3d$ bands. The $Z+1$ approximation leads to a wrong peak position of the second peak in the L_3 edge, which appears closer to the first peak than to the third one. This points out that the treatment of the $2p$-core hole within a $Z+1$ approximation fails to reproduce the peak structure of L edges. Therefore, the calculations will be carried out only for the K edges of oxygen. This is not so bad, because as one can see at the results, the interesting orientation dependence is only within the K edge observed.

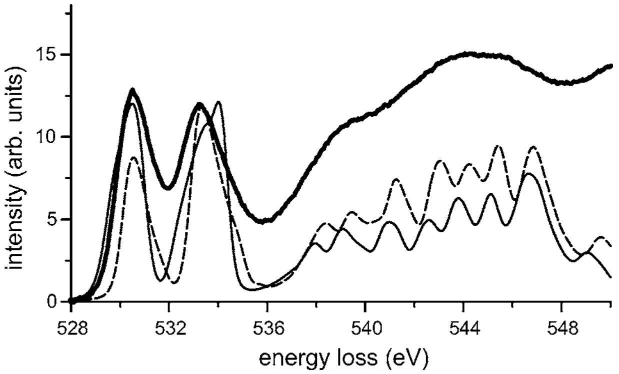

FIG. 7. Influence of the core hole for the oxygen K edge of brookite using the imaging mode and an [100] orientation of the sample surface; thick solid line: experimental data; thin solid line: calculation without core hole; and dashed line: using a $Z+1$ approximation.

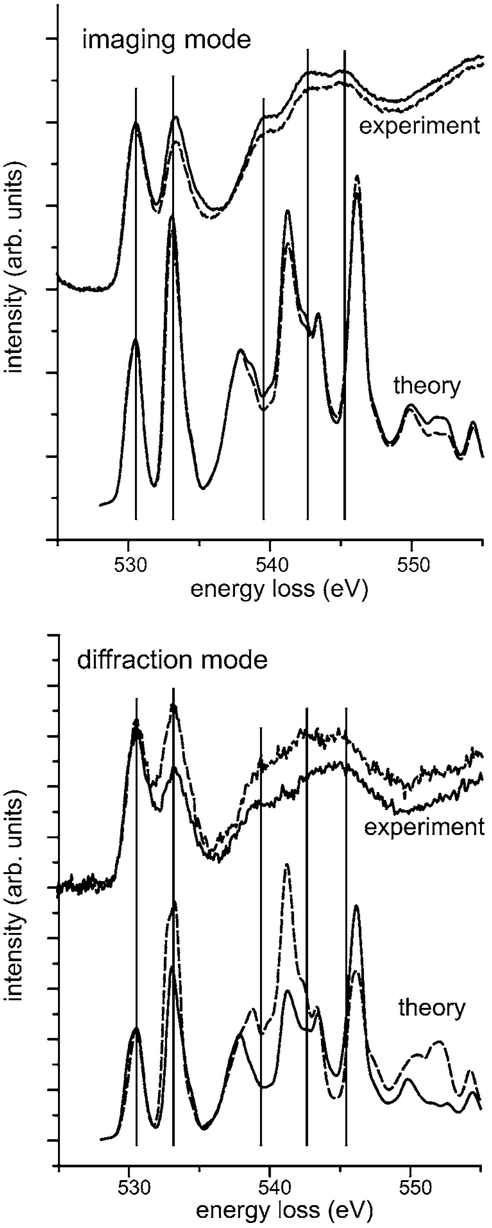

FIG. 8. Orientation dependence of the oxygen K edge for rutile (solid line: [100] direction of the sample surface, dashed line: [001] direction of the sample surface). Top: using a collector semiangle of 13 mrad and a divergence semiangle of 28 mrad; bottom: using a collector semiangle of 3.3 mrad and a divergence semiangle of $<10^{-2}$ mrad.

The importance of the core hole increases in anatase and brookite. One can see this influence in Fig. 7 for brookite for the calculation without core hole and within a $Z+1$ approximation for the oxygen K edge. The influence of the core hole on the titanium L edges is much stronger than for the oxygen K edge, where one can reach a satisfactory agreement already without core hole. However, with core hole the results

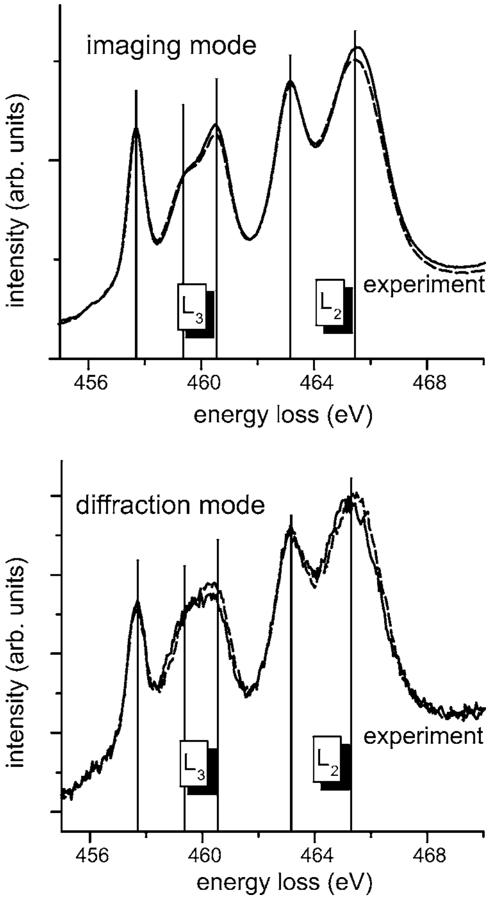

FIG. 9. Orientation dependence of the titanium *L* edges for rutile (solid line: [100] direction of the sample surface, dashed line: [001] direction of the sample surface); top: using a collector semiangle of 13 mrad and a divergence semiangle of 28 mrad; bottom: using a collector semiangle of 3.3 mrad and a divergence semiangle of $<10^{-2}$ mrad.

can be improved. Discrepancies in the oxygen *K* edge above 536 eV are discussed below.

Treating the core hole, a supercell calculation is performed. The supercells used for rutile and anatase are $2\times2\times2$ primitive cells which leads to 48 atoms plus 64 empty spheres per supercell. We also checked for rutile a $3\times3\times3$ supercell but there were no significant changes in the spectra. The used cell sizes are comparable to the cell size of Ref. 37. A large number of atoms in the unit cell limits the size of the supercell. For brookite we have 24 atoms plus 36 empty spheres per primitive unit cell. All atoms are unequal within the core hole treatment. Nevertheless, the distances between two excited atoms are in every direction comparable to the distances in the rutile and anatase supercells. Therefore, we performed the calculations of brookite with the primitive cell.

The finite lifetime of the core hole leads to a broadening of the observed spectrum. Therefore, the calculated spectra are convoluted with a Lorentz function. The full width at half maximum (FWHM) of the Lorentz function used is 0.5 eV for the oxygen *K* edge.[38]

An additional broadening is necessary to account for the experimental energy resolution. Therefore, a convolution with a Gauss function with 0.5 eV FWHM was finally applied to each spectrum.

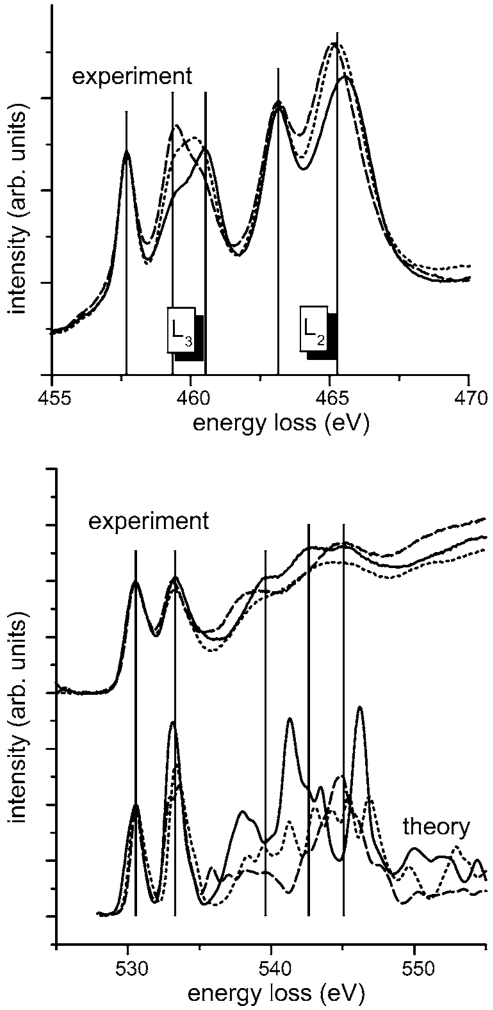

FIG. 10. Comparison of the three crystal modifications oriented in [100] direction of the sample surface (solid line: rutile, dashed line: anatase, dotted line: brookite) using a collector semiangle of 13 mrad and a divergence semiangle of 28 mrad (imaging mode); top: titanium *L* edges; bottom: oxygen *K* edge.

VI. RESULTS

A. Orientation dependence of rutile

In Fig. 8, one can see the orientation dependence of the oxygen *K* edge for rutile. The experimental results measured in both modes, the imaging and the diffraction one, which have been described in Sec. II B, are presented in comparison with the calculated spectra. A very good agreement in the positions of the first two peaks is obtained. The ratio of the intensities of these peaks is not well reflected, which might be due to many-particle effects, namely, the approximation of the core hole. Nevertheless, a very good agreement of the trend in the orientation dependence is observed. As expected, the orientation dependence in the diffraction mode is much more pronounced than in the imaging mode. One has to keep in mind that the main information in the imaging mode is obtained at an angle of 67° to the orientation of the sample surface. That is, the results in the imaging mode with the orientation of the sample surface in [100] direction are related to the results in the diffraction mode with the orientation of the sample surface in [001] direction.

The high energy peaks of the K edge do not show such a characteristic orientation dependence, especially when one keeps in mind that the intensities of these peaks are very sensitive to the background fitting of the experimental data. That is, no differences in the structure are visible. The corresponding calculations reproduce the peak structure, but not the underlying background. This is related to our band structure description due to convergence problems for the high energy region.[12] Similar problems occurred in other theoretical calculations.[11]

The investigation of the orientation dependence of the titanium L edges causes no characteristic difference in the experimental spectra, which is shown in Fig. 9.

No new features were observed for the other two structures. We obtained the same orientation dependence in the oxygen K edge.

B. Comparison of rutile, anatase, and brookite

Figure 10 shows the titanium L edges and the oxygen K edge for all three structures, obtained in the imaging mode. We observe a characteristic difference in the titanium L_3 edge. The ratio of the intensities of the second and the third peak varies for the three crystal modifications. Therefore, one can distinguish between these structures by analyzing the L_3 edge, but one needs a high energy resolution. The measured spectra are in good agreement with other measurements of rutile,[39,40] anatase,[40] and brookite.[1]

For the oxygen K edge, there is no characteristic difference observed in the first two peaks. The multiple scattering part of this edge shows some differences, which can be used to distinguish between the three structures.[41] The calculations confirm this behavior, but do not allow a quantitative description.

VII. CONCLUSION

We have shown that the consideration of the spin orbit coupling of the ground state leads to a distinction between the L_2 and L_3 edge. The important influence of the scattering geometry and the related experimental treatment were discussed. The experimental spectra confirmed this influence, which results in a much higher effect of the orientation dependence in the diffraction mode and can explain the observed spectra in the imaging mode. The imaging mode contains less information about scattering directions lying parallel to the surface normal of the sample. A very good agreement with the calculated spectra was achieved by consideration of the oxygen core hole within a $Z+1$ approximation. Additionally, the experimental collector and divergence semiangles and the tilting of the beam have been taken into account. The used approximations of the core hole lead to a very good agreement in the peak positions, but the relative intensities cannot be reproduced, which is related to the approximate description of the core hole.

---

*Electronic address: christian.heiliger@physik.uni-halle.de

[1] S. Lazar, G. A. Botton, M.-Y. Wu, F. D. Tichelaar, and H. W. Zandbergen, Ultramicroscopy **96**, 535 (2003).

[2] R. F. Egerton, *Electron Energy-Loss Spectroscopy in the Electron Microscope*, 1st ed. (Plenum Press, New York, 1986).

[3] R. D. Leapman, P. L. Fejes, and J. Silcox, Phys. Rev. B **28**, 2361 (1983).

[4] C. Hébert-Souche, P.-H. Louf, P. Blaha, M. Nelhiebel, J. Luitz, P. Schattschneider, K. Schwarz, and B. Jouffrey, Ultramicroscopy **83**, 9 (2000).

[5] C. Souche, B. Jouffrey, G. Hug, and M. Nelhiebel, Micron **29**, 419 (1998).

[6] M. Nelhiebel, P.-H. Louf, P. Schattschneider, P. Blaha, K. Schwarz, and B. Jouffrey, Phys. Rev. B **59**, 12807 (1999).

[7] P. Rez, J. R. Alvarez, and C. Pickard, Ultramicroscopy **78**, 175 (1999).

[8] R. Brydson, J. Phys. D **29**, 1699 (1996).

[9] X. Weng and P. Rez, Phys. Rev. B **39**, 7405 (1989).

[10] S. Köstlmeier and C. Elsässer, Phys. Rev. B **60**, 14025 (1999).

[11] P. Rez, J. M. MacLaren, and D. K. Saldin, Phys. Rev. B **57**, 2621 (1998).

[12] P. Rez, J. Bruley, P. Brohan, M. Payne, and L. A. J. Garvie, Ultramicroscopy **59**, 159 (1995).

[13] L. Landau and E. Lifschitz, *Lehrbuch der Theoretischen Physik, Vol. Bd. 3: Quantenmechanik* (Akademie-Verlag, Berlin, 1979).

[14] H. Bethe, Ann. Phys. **5**, 325 (1930).

[15] M. Inokuti, Rev. Mod. Phys. **43**, 297 (1971).

[16] P. Schattschneider, M. Nelhiebel, and B. Jouffrey, Phys. Rev. B **59**, 10959 (1999).

[17] D. K. Saldin and Y. Ueda, Phys. Rev. B **46**, 5100 (1992).

[18] T. Hahn, *International Tables for Crystallography* (D. Reidel, Dordrecht, 1985).

[19] S.-D. Mo and W. Y. Ching, Phys. Rev. B **51**, 13023 (1995).

[20] B. Poumellec, P. J. Durham, and G. Y. Guo, J. Phys.: Condens. Matter **3**, 8195 (1991).

[21] K. M. Glassford and J. R. Chelikowsky, Phys. Rev. B **45**, 3874 (1992).

[22] M. A. Khan, A. Kotani, and J. C. Parlebas, J. Phys.: Condens. Matter **3**, 1763 (1991).

[23] R. Asahi, Y. Taga, W. Mannstadt, and A. J. Freeman, Phys. Rev. B **61**, 7459 (2000).

[24] P. E. Batson, C. H. Chen, and J. Silcox, Phys. Rev. Lett. **37**, 937 (1976).

[25] R. Tank, O. Jepsen, A. Burkhardt, and O. K. Andersen, *The TB-LMTO-ASA Programm* (1995), LMTO 47 manual.

[26] K. Kokko, R. Laihia, and W. Hergert (private communication).

[27] K. Lie, R. Brydson, and H. Davock, Phys. Rev. B **59**, 5361 (1999).

[28] T. Mizoguchi, I. Tanaka, M. Yoshiya, F. Oba, K. Ogasawara, and H. Adachi, Phys. Rev. B **61**, 2180 (2000).

[29] G. Duscher, R. Buczko, S. J. Pennycook, and S. T. Pantelides, Ultramicroscopy **86**, 355 (2001).

[30] S. Nufer, T. Gemming, C. Elsässer, S. Köstlmeier, and M. Rühle, Ultramicroscopy **86**, 339 (2001).

[31] F. M. F. de Groot, J. Faber, J. J. M. Michiels, M. T. Czyzyk, M. Abbate, and J. C. Fuggle, Phys. Rev. B **48**, 2074 (1993).

[32] F. M. F. de Groot, J. C. Fuggle, B. T. Thole, and G. A. Sawatzky, Phys. Rev. B **41**, 928 (1990).

[33] K. Ogasawara, T. Iwata, Y. Koyama, T. Ishii, I. Tanaka, and H. Adachi, Phys. Rev. B **64**, 115413 (2001).

[34] G. van der Laan and B. T. Thole, Phys. Rev. B **43**, 13401 (1991).

[35] P. L. Potapov, K. Jorissen, D. Schryvers, and D. Lamoen, Phys. Rev. B **70**, 045106 (2004).

[36] J. Luitz, M. Mayer, C. Hbert, P. Schattschneider, P. Blaha, K. Schwartz, and B. Jouffrey, Eur. Phys. J. B **21**, 363 (2001).

[37] C. Elsässer and S. Köstlmeier, Ultramicroscopy **86**, 325 (2001).

[38] P. Skytt, P. Glans, K. Gunnelin, J. Guo, and J. Nordgren, Phys. Rev. A **55**, 146 (1997).

[39] C. Mitterbauer, G. Kothleitner, W. Grogger, H. Zandbergen, B. Freitag, P. Tiemeijer, and F. Hofer, Ultramicroscopy **96**, 469 (2003).

[40] R. Brydson, H. Sauer, W. Engel, J. M. Thomas, E. Zeitler, N. Kosugi, and H. Kuroda, J. Phys.: Condens. Matter **1**, 797 (1989).

[41] H. Sauer (private communication).